Published in final edited form as:
IEEE Trans Biomed Eng. 2010 January ; 57(1): 93–102. doi:10.1109/TBME.2009.2028150.

Adaptive Transthoracic Refocusing of Dual-Mode Ultrasound Arrays

John R. Ballard [Student Member, IEEE],
Department of Electrical and Computer Engineering, University of Minnesota, Twin Cities, MN 55455 USA

Andrew J. Casper [Student Member, IEEE],
Department of Electrical and Computer Engineering, University of Minnesota, Twin Cities, MN 55455 USA

Yayun Wan [Student Member, IEEE], and
Department of Electrical and Computer Engineering, University of Minnesota, Twin Cities, MN 55455 USA

Emad S. Ebbini [Senior Member, IEEE]
Department of Electrical and Computer Engineering, University of Minnesota, Twin Cities, MN 55455 USA

John R. Ballard: ball0250@umn.edu; Andrew J. Casper: casp0069@umn.edu; Yayun Wan: wanx0028@umn.edu; Emad S. Ebbini: emad@umn.edu

Abstract

We present experimental validation results of an adaptive, image-based refocusing algorithm of dual-mode ultrasound arrays (DMUAs) in the presence of strongly scattering objects. This study is motivated by the need to develop noninvasive techniques for therapeutic targeting of tumors seated in organs where the therapeutic beam is partially obstructed by the ribcage, e.g., liver and kidney. We have developed an algorithm that takes advantage of the imaging capabilities of DMUAs to identify the ribs and the intercostals within the path of the therapeutic beam to produce a specified power deposition at the target while minimizing the exposure at the rib locations. This image-based refocusing algorithm takes advantage of the inherent registration between the imaging and therapeutic coordinate systems of DMUAs in the estimation of array directivity vectors at the target and rib locations. These directivity vectors are then used in solving a constrained optimization problem allowing for adaptive refocusing, directing the acoustical energy through the intercostals, and avoiding the rib locations. The experimental validation study utilized a 1-MHz, 64-element DMUA in focusing through a block of tissue-mimicking phantom [0.5 dB/(cm·MHz)] with embedded Plexiglas ribs. Single transmit focus (STF) images obtained with the DMUA were used for image-guided selection of the critical and target points to be used for adaptive refocusing. Experimental results show that the echogenicity of the ribs in STF images provide feedback on the reduction of power deposition at rib locations. This was confirmed by direct comparison of measured temperature rise and integrated backscatter at the rib locations. Direct temperature measurements also confirm the improved power deposition at the target and the reduction in power deposition at the rib locations. Finally, we have compared the quality of the image-based adaptive refocusing algorithm with a phase-conjugation solution obtained by direct measurement of the complex pressures at the target

---

Correspondence to: John R. Ballard, `ball0250@umn.edu`.

Color versions of one or more of the figures in this paper are available online at http://ieeexplore.ieee.org.

location. It is shown that our adaptive refocusing algorithm achieves similar improvements in power deposition at the target while achieving larger reduction of power deposition at the rib locations.

Index Terms

Adaptive beamforming; high-intensity focused ultrasound (HIFU); phased arrays; therapeutic ultrasound; ultrasonic imaging

I. INTRODUCTION

High-intensity focused ultrasound (HIFU) continues to receive increased attention as a therapeutic tool in the treatment of cancer and other tissue abnormalities. HIFU offers some unique advantages as a form of nonionizing radiation suitable for the localized treatment of deep-seated tumors in a noninvasive or minimally invasive manner [1]. Image guidance using diagnostic MRI [2] and ultrasound [3] has led to increased acceptance of HIFU as a noninvasive therapeutic tool. Currently, HIFU is approved worldwide for use in the treatment of uterine leimyomas [4] and prostate cancer [5]. The HIFU beam experiences minimum distortion when focusing at the target sites by utilizing a noninvasive probe for the treatment of the uterine leimyomas and an intracavitary transducer for the prostate [4], [5]. During the treatment session, image guidance is vital to target the treatment location and to avoid the potential for collateral damage to the intervening tissue in the path of the HIFU beam. Temperature-sensitive MRI has been used in monitoring the application of HIFU in the treatment of uterine fibroids, and ultrasound has been shown to provide adequate feedback in guiding the HIFU treatment of prostate cancer. Other systems employing ultrasound-guided HIFU in the treatment of a variety of tumors are also being investigated.

Current clinical HIFU systems employ concave mechanically scanned transducers with relatively low f_{number} (to provide high focusing gain). Both single-element and (coarsely sampled) array transducers are being used. Array transducers for generating HIFU beams offer additional advantages of compensating for tissue heterogeneities in the path of the HIFU beam [6]–[13]. Depending on the size and distribution of the array elements, amplitude and/or phase compensation of the driving signals to the elements can be used to refocus the HIFU beam at the target in the presence of tissue aberrations. This, of course, assumes that information about tissue aberration is reliably measured or estimated. One way to estimate these aberrations is by using 3-D numerical modeling of the acoustic wave propagation based on tissue parameters from pretreatment X-ray computed tomography (CT) or MRI patient datasets [14], [15]. This approach has been suggested for focusing HIFU beams through the skull, but it will be of limited value when targeting tumors in abdominal organs where motion is significant. Alternatively, implantable hydrophones can be used to measure the array directivity at or near the target and refocus the beam based on phase-conjugation or time-reversal methods [16]. This approach was suggested for focusing hyperthermia arrays where the acoustic sensors can be integrated with the necessary temperature sensors, but it is less attractive in HIFU applications where the use of temperature sensors is not mandated.

We have recently introduced the concept of dual-mode ultrasound array (DMUA) systems for image-guided application of therapeutic HIFU [17]–[21]. The advent of piezocomposite transducer technology has provided us with new generation of transducers capable of producing high-power levels suitable for therapy with reasonably wide bandwidth suitable for imaging [22]. Furthermore, piezocomposite technology results in array elements with low lateral cross-coupling leading to more predictable element and beam patterns, both in imaging and therapy modes. We have investigated a number of approaches for improving the image quality of a prototype DMUA that was originally optimized for therapeutic performance [23], [24], including conventional imaging in sector scan format [25] and Cartesian coordinates using synthetic aperture (SA) and single transmit focus (STF) imaging [17], harmonic and nonlinear quadratic imaging [26], nonlinear frequency compounding [18], and the use of coded excitation with pseudoinverse filtering to balance axial and lateral resolution [24], [27].

In this paper, we address the problem of using DMUAs in targeting tumors in organs where the HIFU beam is partially obstructed by the ribcage, e.g., liver and kidney tumors. This is illustrated in Fig. 1, which shows a converging HIFU beam to a focal point in a liver tumor based on homogeneous field calculations. The challenge is to achieve a specified therapeutic dose at the target focus (within the tumor) while minimizing high-power exposure to the ribs. Heating of the ribs and their immediate surroundings is likely to be significantly higher than the normal tissue due to increased absorption of the transmitted wave, increased reflection due to the impedance mismatch, and potential mode conversion due to the tissue–solid interface. The latter could compound the heating problem due to high local absorption of shear waves in the soft tissue [28]. Our approach to this problem takes advantage of the inherent registration between the imaging and therapeutic coordinate systems of the DMUA by identifying (approximately) the rib and target locations from gray-scale SA or STF images. Since the same beamforming parameters are used in imaging and therapy, the estimate of the rib location is valid even in the presence of tissue aberrations. The DMUA element directivities at the rib locations and the target are estimated from the beamforming parameters. From the element directivities, we form array directivity vectors to the target and a set of critical points at the rib locations. The array directivity vectors provide all the necessary information for solving the constrained optimization problem of finding the complex excitation vector that achieves a specified power deposition level at the target while minimizing the power deposition at the critical points. The complex array excitation vector is used to compute the delay profiles necessary to obtain STF images of the treatment region at diagnostic levels. Backscatter from the rib locations in response to these test patterns provides feed-back on the success of the refocusing algorithm in reducing the incident power at the rib locations.

It must be emphasized that DMUA imaging is the key to both the identification of the critical points and the assessment of the quality of the refocused beams in terms of minimizing the power deposition at these locations. The latter represents a unique advantage of the approach described in this paper as STF imaging provides immediate feedback on the power deposition to the critical points. The integrated backscatter from these locations can be obtained within the acquisition time of a single STF frame time for a given test pattern (100–200 μs). This allows for the transmission and assessment of multiple test patterns within very short intervals $\mathcal{O}$(1 ms). Thus, it will be possible to obtain this diagnostic-level feedback without any significant interruption to the treatment protocol and at acquisition rates that will allow for motion tracking in real time. This cannot be matched by any other form of image guidance by a separate diagnostic imaging system. However, we also emphasize that we do not claim that our approach will eliminate the need for separate diagnostic image-guidance system, but provides key feedback features in terms of monitoring and control of the HIFU beam directly at the target and any significant critical points in its path.

II. MATERIALS AND METHODS

A. Dual-Mode Ultrasound Array Prototype

A 64-element, 1-MHz, linear concave array on a spherical shell (100 mm radius) has been designed and fabricated using HI-1 piezocomposite technology (Imasonic, Besançon, France) [22] for HIFU applications, which is available in our laboratory. Each element in the DMUA has an elevation of 50 mm and pitch of 2.0 mm. The DMUA prototype has a low f_{number} of 0.8 in order to maximize the array focusing gain in the intended therapeutic operating field (ThxOF), and is sampled spatially at $1.33\bar{3}\lambda$. spacing in the lateral direction that results in grating lobes, which we have previously established through computer simulation, and are kept at least 25 dB below the focus for every point within the ThxOF [21], [24]. In therapeutic mode, the array has shown to produce up to 250 W with efficiency ≈60% with a 37% bandwidth around the center frequency of 1.1 MHz [21]. In pulse-echo mode without matching, the DMUA has two predominant resonance frequencies at 1.1 and 2.1 MHz. These characteristics are consistent with an earlier prototype that was described in [24] and [25].

B. Instrumentation

We have designed and built a DMUA driver system employing amplifier boards and matching circuitry allowing for pulsed-wave (PW) and continuous-wave (CW) operation at 1 MHz. A Spartan3 field-programmable gate array (FPGA) (XC3S200, Xilinx, Inc., San Jose, CA) is used to generate control signals and driving patterns for the DMUA prototype. The current driver runs at a 300-MHz clock allowing for ≈0.0067 V_{dc} and 1.2° amplitude and phase resolutions, respectively.

The DMUA elements were connected to a transmitter and a receiver through a diplexer and a 4 × 64 matrix switch (Tektronix, Beaverton, OR). A pulser/receiver (Panametrics 5800, GE, Fair-field, CT) was connected to the receive terminals on the matrix switch with the receiver connected to a 20-Msample/s 23-bit digitizer (E1437A, Agilent, Santa Clara, CA). For field scan measurements, a hydrophone (TNU001A, NTR, Seattle, WA) was used with a 30-dB preamplifier connected to a three-stage position system. The instrumentation was controlled utilizing software developed in MATLAB (Instrument Control Toolbox, Mathworks, Natick, MA).

C. Target Volume

To demonstrate the feasibility of the adaptive focusing method, we designed a tissue-mimicking phantom with four embedded Plexiglas ribs (9.25 mm in diameter) spaced 16 mm apart to simulate the rib cage. The phantom measured 90 mm × 70 mm × 65 mm and was fabricated from gelatin, glutaraldehyde, graphite, propanal, and water, as suggested in [29]. For the purposes of this paper, the phantoms served as an attenuating [0.45 dB/(MHz·cm)] speckle-generating medium. The phantom is 2-D due to the nature of the 1-D 64-element array used to image and provide therapy. A 1.5-mm-diameter needle thermocouple (OMEGA Engineering, Stamford, CT) was used as a target in the ThxOF of the DMUA with an additional 1.5 mm needle thermocouple(s) placed on the rib(s) in the simulated rib cage. The thermocouple measurements were taken at a rate of 200 Hz using a data acquisition unit (34970A, Agilent, Santa Clara, CA). A diagram of the experimental setup is shown in Fig. 2.

D. Image Formation

B-mode images of the phantom were formed using SA beam-forming and STF imaging. STF images were taken before and after employing the refocusing algorithm using the setup described before.

1) Synthetic Aperture Imaging—

SA images were obtained by using the full SA technique with two-way (transmit-and-receive) dynamic focusing [30]. The SA images are among the highest quality conventional image from any given array [30]. The echo signal from each pixel location is computed by [26]

$$I(x_p, z_p)=\sum_{i=1}^{64}\sum_{j=1}^{64} A_i B_i s_{i,j}\left[\frac{R_{ip}+R_{jp}}{c}\right] \tag{1}$$

where c is the speed of sound, A_i and B_j are, respectively, the transmit and receive apodization weights, R_{ip} and R_{jp} are, respectively, the distances from the transmitting and receiving elements to the image pixel P, and $s_{i,j}$ (t) is the echo received by element j when transmitting with element i.

2) Single Transmit Focus Imaging—STF imaging is a modified version of (1) where we image with the pulsed (one to two cycles duration) therapeutic beam as the transmit imaging focus at diagnostic intensity levels. To form a 2-D image throughout the DMUA imaging field of view, dynamic receive focusing is used, which in a uniform speckle region amounts to imaging the therapeutic beam. This imaging mode allows for the visualization (and possible characterization) of strongly scattering objects in the path of the HIFU beam (e.g., bone) at safe diagnostic levels. It provides an imaging method for surveying the treatment volume at diagnostic levels before the therapeutic HIFU beam is applied. The image formation equation for STF images is as follows:

$$I(x_p, z_p)=\sum_{j=1}^{64} B_j s_j \left[\frac{R_{wp}+R_{jp}}{c}\right] \tag{2}$$

where s_j is the received waveform at element j, and R_{wp} is the minimum distance between the leading edge of the converging wavefront of the STF and pixel P at the time $t = 0$. All other quantities are the same as their counterparts in (1).

E. Adaptive Refocusing Algorithm Design

The B-mode image provides feedback for the determination of target and critical points. The objective of adaptive focusing is to maximize the array intensity gain at a target point(s) $\vec{r}_T$, while minimizing across a set of critical points $\vec{r}_T(i)$, $i = 1, 2, \ldots, M_C$. This becomes an optimization problem, which can be solved using Lagrange multipliers or a regularized minimum-norm least squares solution [31] utilizing the pseudoinverse method [23]. In order to solve the optimization problem, the element directivities at the target and critical points must be known. This is generally not the case without direct measurements (e.g., using implantable hydrophones [16]) or detailed computational models for wave propagation in inhomogeneous media [13], [14]. However, these directivities can be estimated from the beamforming parameters used in forming STF or SA images of the treatment region. From these measurements, we define a vector h_t from the N-element array to the target location(s) by the array directivity vectors $h_k(\vec{r}_T)$, $k = 1, 2, \ldots, N$

$$\mathbf{h}_t=[h_1(\vec{r}_T), h_2(\vec{r}_T), \ldots, h_N(\vec{r}_T)]. \tag{3}$$

Likewise, vectors from the array to each critical location $\mathbf{h}_i$ are defined by the array directivity vectors. A matrix $\mathbf{H}_C$ is the collection of these vectors from the critical locations

$$\mathbf{h}_i=[h_1(\vec{r}_C(i)), h_2(\vec{r}_C(i)), \ldots, h_N(\vec{r}_C(i))]. \tag{4}$$

The weighting matrix $\mathbf{W}_C$ is formed with the matrix of critical directivity vectors and an appropriately chosen regularization parameter γ as follows:

$$\mathbf{W}_C=[\mathbf{H}_C^{*t}\mathbf{H}_C+\gamma\mathbf{I}]^{-1}. \tag{5}$$

Our selection of γ was the smallest nonzero singular value of the singular value decomposition of $\mathbf{H}_C$. This leads to the optimal complex array excitation vector for the weighted minimum-norm solution as follows:

$$\widehat{\mathbf{u}}=\mathbf{W}_c\mathbf{h}_T^{*t}(\mathbf{h}_T\mathbf{W}_C\mathbf{h}_T^{*t})^{-1}p_0 \tag{6}$$

where p_0 is the specified complex pressure at the target. Note that, for a single focus at the target, p_0 is a scalar and $\mathbf{h}_T^{*t}$ is a row vector. For the multiple-focus case, these will be expressed as a vector of complex pressures and a matrix of element directivity vectors, respectively.

As outlined in Section I, the element directivity vectors at the target and critical points can be estimated from the beamforming parameters in the imaging mode. Either SA or STF imaging can be used to estimate these quantities from the imaging coordinates. STF imaging is used in the assessment of the reduction of power deposition at the critical points.

III. RESULTS

We describe an experimental study to validate our image-based adaptive refocusing algorithm in the presence of strongly scattering obstacles in a speckle-generating phantom, as shown in Fig. 2. This section is organized around the three aspects of the proposed method: 1) the identification of the target and critical points from SA or STF images and the application of the adaptive refocusing algorithm. Direct temperature measurements at the target and rib locations are used to assess the resulting changes in power deposition; 2) the use of STF imaging to provide feedback about the power deposition to the ribs upon refocusing. Experimental results relating the integrated back scatter from rib locations to the directly measured temperatures are presented; and 3) acoustic characterization of the HIFU beam distribution at the DMUA surface, rib plane, and target plane. The results of the image-based refocusing algorithm are compared with the results of refocusing based on direct hydrophone measurements of the element directivities at the target location [16]. These results demonstrate that our refocusing algorithm produces well-behaved field patterns with well-behaved array excitation vectors, i.e., the inverse problem solved by (6) is well posed.

A. Image-Based Adaptive Refocusing

1) Image Guidance—Fig. 3 shows the SA image (50 dB) of the phantom with the target at the geometric focus (0 mm lateral, 100 mm axial) with the ribs visible at an axial distance of 55 mm. Note that the application of the algorithm does not require a strong scatterer at the target location. In this paper, we used the thermocouple as a scatterer at the target location to demonstrate the relation between changes in echogenicity and temperature change upon refocusing. It is interesting to note that the image of the target in this image appears quite diffuse with high lateral sidelobes. This is due to beam distortions that were not taken into account in the SA beamforming algorithm. Compared to the image of the target in the absence of the ribs (not shown), this distortion is quite pronounced as one might expect. Nonetheless, the image suggests that the DMUA still achieves certain level of focusing around the target. Based on the image shown, four critical points at the (approximate) center of each rib were chosen in addition to the target point. The matrix $\mathbf{H}_c$ was formed by using the array directivity vectors in the vicinity of each critical point. Specifically, for each critical point, we have computed the array directivity vectors for a set of points covering the extent of the corresponding rib in the lateral direction with spatial sampling of λ/2, where λ is the operating wavelength in the soft tissue (1.5 mm in this case). The array directivity vector at the target $\mathbf{h}_T^{*t}$ is also obtained from the beamforming parameters at the target point, i.e., without correcting for the inhomogeneity presented by the ribs.

The estimated array directivity vectors were used to refocus the DMUA at the target in the presence of the ribs. Before applying the HIFU beam for therapeutic heating, the DMUA was driven with a diagnostic-level excitation vector resulting from (6) in the pulse mode to obtain STF images of the target medium upon refocusing. Fig. 4 shows STF images (50 dB) of the target region and the ribs using: 1) the geometrically focused HIFU beam (assuming homogeneous medium) and 2) the refocused HIFU beam according to (6). The two images are normalized to the same maximum intensity for comparison purposes. One can see that the echogenicity of the ribs is lower in the refocused image with respect to the echogenicity of the target.

Fig. 5 further illustrates the change in relative echogenicity at the middle rib locations upon refocusing. The line plots show the echogenicity profiles along an axial line through the target [Fig. 5(a)] and two axial lines through the two central ribs [Fig. 5(b) and (c)]. The solid lines are obtained from the image in Fig. 4(a) and the dashed lines are obtained from Fig. 4(b). The results clearly show that while the relative echogenicity of the target is the same for both HIFU beams, the echogenicity of the ribs drops measurably (6–10 dB) upon refocusing. This result suggests that STF imaging can be used as an early indicator of the success of the refocusing algorithm in lowering the power deposition at the rib locations.

To further demonstrate the usefulness of the feedback provided by the STF imaging using diagnostic-level HIFU beams, we show a summary of the experimental results of refocusing when targeting points 5 and 10 mm laterally off the DMUA geometric center in Section III-A3.

2) Direct Temperature Measurements—Temperature measurements were taken at the target and rib location(s) before, during, and after a 4-s HIFU exposure. This was done for both the geometrically steered and refocused driving patterns for all three target locations given before. For each case, the dc power delivered to the DMUA was normalized for the adaptively and geometrically focused driving patterns. Furthermore, to show repeatability, each measurement was taken a minimum of five times. The results shown in Fig. 6 show a comparison of normalized temperature change (and variance) at the target and one rib location for the geometrically focused and adaptively refocused driving patterns when the target is at the geometric focus. The temperatures are normalized with respect to the maximum temperature at the target resulting from the geometrically focused HIFU beam. One can see that using the refocused HIFU beam increased the temperature at the target by 65%. At the same time, it decreased the temperature at the rib by nearly 80%. In this case, the target to rib temperature ratio T_T/T_{rib} was increased from 0.94 to 6.1. Table I shows the relative temperature change across both the middle ribs as well as at the target location for the cases when the target point is located at (5, 100) and (10, 100) mm, respectively. These results show that the relative temperature increase at the target upon refocusing varies depending on the location of the target with respect to the ribs. Similarly, the degree of relative decrease in temperature at the ribs also varies for the different cases. It is, however, important to note that the trends shown by these results are quite general in that the application of the adaptive refocusing always results in increasing the power deposition at the target and reduction in power deposition at the ribs.

3) Summary of Temperature and Echogenicity Changes—The STF imaging results shown before suggest that changes in the echogenicity at the target and rib locations upon adaptive refocusing agree with the measured temperature changes at these locations. Table I summarizes these changes in terms of the temperature ratio T_T/T_{rib} for each case. We also report the measured echogenicity from the normalized STF images for each case. For the adaptive refocusing cases, we show the relative change in target to rib echogenicity in decibels defined as follows:

$$\Delta E = 10\log_{10}\left[\frac{E_{TR}/E_{TG}}{E_{RR}/E_{RG}}\right]$$

where E_{TG} (E_{RG}) and E_{TR} (E_{RR}) are the integrated backscatter values from the target (rib) location due to the geometrically focused and the adaptively refocused HIFU beams. The integrated backscatter measurement is formed from the average of five beamformed A-lines centered at the location of interest. One can see that the relative changes in echogenicity appear to have the same trend as the relative changes in temperature ratios. While this is currently not a quantitative measurement, it suggests a monotonic relationship between temperature change (a measure of power deposition) and the integrated backscatter. This relationship allows the use of STF to provide immediate feedback from the target and rib locations on the increase/ decrease in power deposition upon refocusing. Given that the frame times of STF imaging is in the 100–200 μs range, this form of feedback allows for testing multiple refocused beams during very short intervals on the order of $\mathcal{O}(1 \text{ ms})$ and choose the best in terms of increasing power deposition at the target while decreasing the power deposition at the rib locations in the path of the HIFU beam. This is illustrated in the next section.

B. Image-Based Feedback on Changes in Power Deposition

The selection of the critical points from gray-scale images involves some level of uncertainty due to the following reasons.

1. The lateral resolution of the imaging system is limited (1.2 mm for the DMUA prototype used).
2. The geometry of the obstacle with respect to the DMUA produces angular scattering functions that may obscure the shape of the obstacle. This is especially true for our DMUA, which has poor axial resolution of ≈2.6 mm. As can be seen from the images shown before, even a strongly scattering object appears amorphous, especially in STF images.
3. The surrounding speckle from the soft tissue may drown the echoes from the obstacle, except for the strongest specular reflection. This is clearly the case in STF images, but is less so in the SA image shown, which appears to capture the top surface of the ribs.

Due to the aforementioned reasons, it may be necessary to test several "refocused" HIFU beams accounting for the uncertainty in the obstacle locations. To demonstrate this, we have varied the estimated position of the critical points associated with one of the middle ribs when focusing at (5, 100) mm. We have used the critical point corresponding to the right rib and varied its position by ±0.5 and ±1 mm. Equation (6) was used to find the excitation vector corresponding to each one of these critical points. We then used these excitation vectors to obtain STF images of the treatment region to measure the changes in rib echogenicity corresponding to each driving vector. Finally, we applied the different excitation vectors in the 4-s therapeutic mode described before and recorded the resulting temperature profiles at the target and the rib. The results of this experiment are summarized in Fig. 7. The figure shows the recorded temperature in Fig. 7(b) and the axial echogenicity profiles in Fig. 7(a) for four of the six cases (to avoid crowding): original critical point with geometric focusing (thick solid), original critical point with refocusing (dotted), shifted critical point (+1 mm) with refocusing (dashed-dotted), and shifted critical point (−1 mm) with refocusing (thin solid). The recorded temperatures are relative to the maximum temperature at the target using the geometrically steered HIFU beam. Fig. 7(c) shows the maximum recorded temperature plotted against the maximum echogenicity for each case. This result demonstrates the feasibility of using STF imaging for providing feedback on reduction/increase in power deposition at a given obstacle resulting from the use of different HIFU beams in focusing at a specific target. This feedback is practically instantaneous. For example, all six STF images can be obtained in approximately 900 μs. With dedicated beamforming and image processing hardware/software, it is possible to select the most appropriate pattern (in terms of maximum power deposition at the target with minimum power deposition at the critical point) within milliseconds. This will have negligible effect on the treatment protocol and will still allow for real-time treatment control, including motion tracking.

C. Acoustic Field Characterization

Additional insight on the workings of the refocusing algorithm is provided by direct measurement of the acoustic field profiles in the rib and target planes for different HIFU excitation vectors in the presence of the ribs. To do this, we placed the ribs in front of the DMUA, as shown in Fig. 2, without the speckle-generating phantom present. A needle hydrophone was used to measure the intensity profiles directly behind the ribs (as seen from the DMUA) and in the target plane in degassed water (3 ppm dissolved oxygen). Three HIFU beams were used: 1) a geometrically focused beam (0, 100); 2) an adaptively focused beam using (6); and 3) a phase-conjugation solution obtained by measuring the complex pressures from the DMUA elements at the target location. Phase conjugation is the spatial matched-filter solution [16], which maximizes the array gain at the measurement point. This measurement amounts to measuring the DMUA element directivities directly at the target point. This is the CW equivalent of the time-reversal solution proposed by Fink and coworkers [13], [32]–[34]. This solution may serve as a gold standard for the refocusing problem described in this paper as it incorporates the full knowledge of the array directivity at the target (subject to measurement error).

Fig. 8 shows the results of this experiment for the three driving patterns. Fig. 8(a) shows the focal plane intensity profiles for the geometrically focused (solid), the adaptively refocused (dotted), and the phase-conjugation refocused (dashed-dotted) HIFU beams. The intensity profiles just behind the ribs (as seen from the DMUA) are shown in Fig. 8(b). All patterns are normalized with respect to the peak intensity of the geometrically focused HIFU beam in the focal plane. One can see that both the adaptively refocused and the phase-conjugation refocused HIFU beams nearly double the focal intensity for the same dc power input to the DMUA. This is a significant improvement in the array gain compensating for the effects of the ribs. Comparison between the two refocused beam profiles not only shows the general agreement between them, but also reveals some subtle differences. In particular, the adaptively refocused HIFU beam relies more on the intercostals in producing the focused field at the target while the phase-conjugation refocused HIFU beam appears to allow for relatively higher partial transmission through the ribs, as shown in Fig. 8(b). The relative distributions of power in the rib plane due to the different refocusing algorithms must be compared in terms of their ability to achieve the specified therapeutic endpoint at the target while minimizing the heating of both the ribs and the intercostals. Our adaptive refocusing approach is based on treating the ribs as critical structures where the power deposition is to be minimized, thus favoring the transmission through the intercostals. This criterion can be modified to allow for some partial transmission through the ribs if it is determined that it will be safe to do so at power levels necessary to achieve a specified intensity gain at the target.

Comparing the focal plane intensity profiles, one observes increased grating lobe levels for all three patterns, but especially for the adaptively refocused HIFU beam. These grating lobes are not due to the DMUA elements sampling. They are due to the presence of a “virtual array” in the intercostals due to the partial blocking of the HIFU beams by the ribs. The height of the grating lobes can be explained by the relative level of partial blocking.

Finally, it is interesting to examine the typical magnitude and phase distributions of the DMUA excitation vector resulting from the application of adaptive refocusing according to (6), as shown in Fig. 9. These distributions resulted from refocusing the DMUA at (5, 100) mm in the presence of the Plexiglas ribs as described before. One can see that all the array elements are activated, even those elements shadowed by the ribs. This is due to the fact that all elements are needed to obtain the highest level of destructive interference at the rib locations while maximizing constructive interference at the target. We have compared our adaptive refocusing based on (6) with a ray tracing solution, which shuts off the DMUA shadowed by the ribs. The results have clearly shown that the ray tracing solution consistently results in higher power deposition at the rib location. Therefore, our adaptive refocusing algorithm intelligently uses all the degrees of freedom (DMUA elements) to meet the constraints at the target while minimizing the power deposition at the ribs.

IV. DISCUSSION

The results presented in this paper are applicable to practical applications based on the current status of imaging with DMUAs. We have previously shown that DMUA imaging in the tissue and speckle-generating quality assurance phantoms produces images that can be compared with those obtained using diagnostic scanners [21] with the following differences.

1. Currently, a typical DMUA with 30% fractional band-width produces images with axial resolution of approximately 2.6 mm, which is significantly poorer than diagnostic probes (generally in the submillimeter range).
2. Due to their large aperture and concave geometry, DMUAs produce excellent lateral resolution typically around 1 mm.

We have shown that improvements in the DMUA image quality can be achieved using coded excitation and pulse-compression inverse filtering together with explicit accounting to some of the element and array geometry in beamforming. However, even without these improvements, results shown in this paper demonstrate the feasibility of identifying strongly scattering structures like the ribs, even when they are embedded in tissue-mimicking phantoms.

Both our SA and STF imaging have been largely based on conventional beamforming, and therefore represent a form of backscatter imaging. With the large-aperture array, SA imaging captures the proximal edge of the ribs, which may allow for reasonable selection of the critical points associated with each obstacle and its extent from the specular reflections. STF images, on the other hand, currently do not capture the geometry of the obstacle, but only the critical point obtained from the dominant specular reflection. This can be appreciated by comparing the specular reflections from the ribs in the SA image in Fig. 3 and the STF image in Fig. 4. One can see a more contiguous specular reflection from the proximal edge of each rib in the SA image as compared to the spot-like specular reflections in the STF image. In practice, this means that we may use SA imaging for the initial survey of the scene to estimate the extent of each obstacle and perform the real-time tracking of the critical point associated with each obstacle using STF imaging. As we have illustrated in Section III-B, uncertainty in the location of the critical point can be overcome by using several test patterns and choosing the one that minimizes the backscatter from the rib location.

The adaptive refocusing algorithm presented in this paper is optimal in the sense of achieving a specified power level at the target while minimizing the power level at the ribs. Comparisons with the phase-conjugation method for refocusing show that both approaches improve the DMUA focusing gain at the target and direct the power flow into the intercostals with minimum differences. These differences primarily stem from the different levels of partial transmission through the ribs, but may be attributed to other factors. For example, the adaptive refocusing method uses the uncorrected array directivity vector h_T as opposed to the measured directivity vector used by the phase-conjugation method. We are currently investigating methods for estimating the array directivity vectors at the target location for use with our refocusing algorithm. We, however, emphasize that the refocusing algorithm compares favorably with the phase-conjugation refocusing method despite the errors in the estimation of h_T.

The use of cylindrical Plexiglas ribs should not be construed as an unrealistic simplification that diminishes the significance of the results reported in this paper. In fact, in comparing SA and STF images of imaging the Plexiglas and real ribs from beef samples, we significantly observed more distortion from the Plexiglas ribs. The Plexiglas ribs are being used for two reasons.

1. The geometry of the current DMUA prototype is fundamentally 1-D, and we wanted to use obstacles that do not vary in the elevation direction to accommodate this limitation. Obviously, this will not be necessary if we had a 2-D or even 1.5-D DMUA (currently being designed).
2. We are also developing a forward scattering model for further validation of our imaging concepts. The cylindrical geometry of the Plexiglas ribs lends itself to closed-form scattering solutions that can be used in validating our forward scattering model.

There are several variations on the current adaptive refocusing algorithm that can be studied, for example, a two-step procedure that performs the synthesis problem in the soft tissue first from a virtual array within the intercostals to the target followed by a second synthesis problem from the physical DMUA to the virtual array. This approach will also allow us to incorporate the partial transmission through the ribs as part of the optimization problem (by extending the virtual array to the distal edges of the ribs). In order to do this meaningfully, however, this approach will need to be developed along with a reliable forward scattering model phase and amplitude distortions due to propagation through bone. The two-step approach is also useful in designing (or configuring) an appropriate DMUA for a given target (defined by the tumor depth and size) and an available discontinuous acoustical window. We are working on developing this approach, together with the forward scattering model mentioned before, to provide a complete solution to the optimization and design of DMUAs for this important application area.

V. CONCLUSION

We have presented experimental verification of an image-based, adaptive transthoracic refocusing algorithm for improved therapeutic targeting of tumors in organs where the HIFU beam is partially obstructed by the ribcage. The results have clearly demonstrated the feasibility of controlling the flow of acoustical power through the intercostals to achieve a specified level of power deposition at the target while minimizing the power deposition at the ribs (critical points). We have also shown that gray-scale STF images provide suitable feedback on the improved quality of the adaptively refocused HIFU beams in terms of lowering the power deposition at the rib locations. This form of feedback is fast (100–200 μs per STF frame) and spatially accurate, especially at the proximal side of the ribs. This allows for several HIFU beams targeting the same point to be tested at subtherapeutic levels below 1 ms to determine which beam produces minimal heating of the ribs in the path of the HIFU beam. In addition, as we have shown previously [21], linear and nonlinear imaging methods using DMUAs can be used to assess tissue response to HIFU lesion formation. Therefore, DMUA imaging provides the necessary feedback to refocus HIFU beams in the presence of strongly scattering structures as well as the assessment of the target tissue to the application of the HIFU beam. This feedback is most valuable due to the inherent registration between the imaging and therapeutic coordinate systems for DMUAs. Together with the results shown in [21], the results shown in this paper demonstrate the promise of the DMUAs in providing a unique paradigm for noninvasive, image-guided surgery.

Acknowledgments

The authors wish to acknowledge P. D. VanBaren (Vibration Research), Dr. C. Simon (Philips), Dr. H. Lee (Medison), and Prof. M.-K. Jeong (Daejin University) for contributions to various aspects of data collection and image formation algorithms used in generating the images presented in this paper.

This work was supported in part by the National Institutes of Health under Grant EB8191.

REFERENCES

1. Sanghvi N, Hynynen K, Lizzi F. New developments in therapeutic ultrasound. IEEE Eng. Med. Biol. Mag 1996 Nov./Dec;vol. 15(no. 6):83–92.
2. Tempany CM, Stewart EA, McDannold N, Quade BJ, Jolesz FA, Hynynen K. MR imaging-guided focused ultrasound surgery of uterine leiomyomas: A feasibility study. Radiology 2003 Nov;vol. 226:897–905. [PubMed: 12616023]
3. Sanghvi NT, Fry FJ, Bihrle R, Foster RS, Phillips MH, Syrus J, Zaitsev AV, Hennige CW. Noninvasive surgery of prostate tissue by high-intensity focused ultrasound. IEEE Trans. Ultrason., Ferroelectr., Freq. Contr 1996 Nov;vol. 43(no. 6):1099–1110.
4. Chan A, Fujimoto V, Moore D, Martin R, Vaezy S. An image-guided high intensity focused ultrasound device for uterine fibroids treatment. Med. Phys 2002;vol. 29:2611–2620. [PubMed: 12462728]
5. Poissonnier L, Chapelon J, Rouviere O, Curiel L, Bouvier R, Martin X, Dubernard J, Gelet A. Control of prostate cancer by transrectal HIFU in 227 patients. Eur. Urol 2007;vol. 51:381–387. [PubMed: 16857310]
6. Chapelon J, Cathignol D, Cain C, Ebbini E, Kluiwstra J, Sapozhikov O, Fleury G, Berriet R, Cupin L, Guy J. New piezoelectric transducers for therapeutic ultrasound. Ultrasound Med. Biol 2000;vol. 26:153–159. [PubMed: 10687803]
7. Pernot M, Berriet R, Aubry J-F, Baron OL, Tanter M, Fleury G, Chupin L, Gallet L, Fink M. High power density prototype for high precision transcranial therapy. Proc. 3rd Int. Symp. Ther. Ultrasound 2003;vol. 1:405–410.
8. Hynynen K, Sun J. Trans-skull ultrasound therapy: The feasibility of using image-derived skull thickness information to correct the phase distortion. IEEE Trans. Ultrason., Ferroelectr., Freq. Control 1999 May;vol. 46(no. 5):752–755. [PubMed: 18238476]
9. Ishida K, Kubota J, Mitake T, Carlson R, Seip R, Sanghvi N, Azuma KST, Kawabata K, Umemura S. Development and animal experiment of variable focusing HIFU system for prostate cancer treatment. Proc. 3rd Int. Symp. Ther. Ultrasound 2003;vol. 1:382–387.
10. Seip R, Chen W, Tavakkoli J, Frizzell L, Sanghvi N. High-intensity focused ultrasound (HIFU) phased arrays: Recent developments in transrectal transducers and driving electronics. Proc. 3rd Int. Symp. Ther. Ultrasound 2003;vol. 1:423–428.
11. Curiel L, Chavrier F, Souchon R, Birer a, Chapelon JY. 1.5-D high intensity focused ultrasound array for non-invasive prostate cancer surgery. IEEE Trans. Ultrason., Ferroelectr., Freq. Control 2002 Feb;vol. 49(no. 2):231–242. [PubMed: 11885680]
12. Martin R, Vaezy S, Chi E. Investigation of HIFU produced emulsion for acoustic hemostasis. Proc. 3rd Int. Symp. Ther. Ultrasound 2003;vol. 1:351–356.
13. Aubry J-F, Pernot M, Marquet F, Tanter M, Fink M. Transcostal high-intensity-focused ultrasound: Ex vivo adaptive focusing feasibility study. Phys. Med. Biol 2008;vol. 53:2937–2951. [PubMed: 18475006]
14. Tanter M, Thomas J, Fink M. Focusing and steering through absorbing and aberrating layers: Application to ultrasonic propagation through the skull. J. Acoust. Soc. Amer 1998;vol. 103:2403–2410. [PubMed: 9604342]
15. Sun J, Hynyen K. Focusing of therapeutic ultrasound through a human skull: A numerical study. J. Acoust. Soc. Amer 1998;vol. 104:1705–1715. [PubMed: 9745750]

16. Seip R, VanBaren P, Ebbini E. Dynamic focusing in ultrasound hyperthermia treatments using implantable hydrophone arrays. IEEE Trans. Ultrason., Ferroelectr., Freq. Control 1994 Sep;vol. 41 (no. 5):706–713. [PubMed: 18263259]
17. Ebbini ES, Bischof JC, Coad JE. Lesion formation and visualization using dual-mode ultrasound phased arrays. Proc. IEEE Ultrason. Symp 2001 Oct;vol. 2:1351–1354.
18. Steidl C, Yao H, Ebbini ES. Dual-mode ultrasound phased arrays for noninvasive surgery: Post-beamforming image compounding algorithms for enhanced visualization of thermal lesions. Proc. IEEE Int. Symp. Biomed. Imag 2002 Jul;:429–432.
19. Yao H, Ebbini ES. Real-time monitoring of the transients of HIFU-induced lesions. Proc. IEEE Ultrason. Symp 2003 Oct;vol. 1:1006–1009.
20. Yao H, Ebbini ES. Dual-mode ultrasound phased arrays for imaging and therapy. Proc. IEEE Int. Symp. Biomed. Imag 2004 Apr;vol. 1:25–28.
21. Ebbini ES, Yao H, Shrestha A. Dual-mode ultrasound phased arrays for image-guided surgery. Ultrason. Imag 2006;vol. 28:201–220.
22. Fleury G, Berriet R, Baron OL, Huguenin B. New piezocomposite transducers for therapeutic ultrasound. Proc. 2nd Int. Symp. Ther. Ultrasound 2002;vol. 1:428–436.
23. Ebbini, E. Ph.D. dissertation. Urbana: Univ. Illinois; 1990. Deep localized hyperthermia with ultrasound phased arrays using the pseudoinverse pattern synthesis method.
24. Wan Y, Ebbini E. Imaging with concave large-aperture therapeutic ultrasound arrays using conventional synthetic-aperature beamforming. IEEE Trans. Ultrason., Ferroelectr., Freq. Control 2008 Aug;vol. 55(no. 8):1705–1718. [PubMed: 18986915]
25. Simon C, Elbakri I, Shen J, Hall T, Ebbini ES. Combined ultrasound image guidance and therapy using a therapeutic phased array. Med. Imag 1998 May;vol. 3341:89–98.
26. Yao H, Phukpattaranont P, Ebbini ES. Enhanced lesion visualization in image-guided noninvasive surgery with ultrasound phased arrays. Proc. 23rd Annu. Int. Conf. IEEE Eng, Med. Biol. Soc 2001 Oct;vol. 3:2492–2495.
27. Shen J, Ebbini ES. Filter-based coded-excitation system for high-speed ultrasonic imaging. IEEE Trans. Med. Imag 1998 Dec;vol. 17(no. 6):923–934.
28. Haken BA, Frizzell LA, Carstensen EL. Effect of mode conversion on ultrasonic heating at tissue interfaces. J. Ultrasound Med 1992;vol. 11:393–405. [PubMed: 1495131]
29. Nightingale KR, Palmeri ML, Nightingale RW, Trahey GE. On the feasibility of remote palpation using acoustic radiation force. J. Acoust. Soc. Amer 2001 Jul;vol. 110:625–634. [PubMed: 11508987]
30. Thomenius K. Evolution of ultrasound beamformers. Proc. IEEE Ultrason. Symp 1996:1615–1622.
31. Botros Y, Ebbini E, Volakis J. Two-step hybrid virtual array-ray (var) technique for focusing through the rib cage. IEEE Trans. Ultrason., Ferroelectr., Freq. Control 1998 Jul;vol. 45(no. 4):989–1000. [PubMed: 18244253]
32. Fink M. Time reversal of ultrasonic fields. I. basic principles. IEEE Trans. Ultrason., Ferroelectr., Freq. Control 1992 Sep;vol. 39(no. 5):555–566. [PubMed: 18267667]
33. Wu F, Thomas J, Fink M. Time reversal of ultrasonic fields. II. Experimental results. IEEE Trans. Ultrason., Ferroelectr., Freq. Control 1992 Sep;vol. 39(no. 5):567–578. [PubMed: 18267668]
34. Prada C, Thomas J, Fink M. The iterative time reversal process: Analysis of the convergence. J. Acoust. Soc. Amer 1995;vol. 95:62–71.

Biographies

John R. Ballard (S'02) received the B.S. degree in electrical engineering in 2005 from Michigan State University, East Lansing, and the M.S. degree in electrical engineering in 2007 from the University of Minnesota, Twin Cities, where he is currently working toward the Ph.D. degree in electrical engineering.

His current research interests include ultrasound imaging and signal processing with special interest in image-guided interventions and high-intensity focused ultrasound therapy.

Andrew J. Casper (S'08) received the B.S. degree in electrical engineering in 2008 from the University of Minnesota, Twin Cities, where he is currently working toward the M.S. degree in electrical engineering.

His current research interests include ultrasound imaging and signal processing with special focus on aberration and large-aperture arrays.

Yayun Wan (S’05) received the B.S. degree in electrical engineering in 2000 from Nanchang University, Nanchang, China, the M.S. degree in physics in 2003 from Bowling Green State University, Bowling Green, OH, and the M.S. degree in electrical engineering in 2006 from the University of Minnesota, Twin Cities, where she is currently working toward the Ph.D. degree in electrical engineering.

Her current research interests include ultrasound imaging and signal processing with special interest in high-frequency ultrasound imaging and image-guided interventions.

Ms. Wan received the Best Paper Award at the 42nd IEEE Design Automation Conference, June 2005.

Emad S. Ebbini (S‘84–M‘85–SM‘07) received the B.Sc. degree in electrical engineering/ communications from the University of Jordan, Amman, Jordan, in 1985, and the M.S. and Ph.D. degrees in electrical engineering from the University of Illinois at Urbana-Champaign, Urbana, in 1987 and 1990, respectively.

From 1990 until 1998, he was on the faculty of the Electrical Engineering and Computer Science Department, University of Michigan, Ann Arbor. Since 1998, he has been with the Electrical and Computer Engineering Department, University of Minnesota, Twin Cities. His current research interests include signal and array processing with applications to biomedical ultrasonics and medical devices.

Dr. Ebbini received the National Science Foundation Young Investigator Award for his work on new ultrasound phased arrays for imaging and therapy. Between 1994 and 1997, he was a member of the AdCom for the IEEE Ultrasonics, Ferroelectrics, and Frequency Control Society. In 1996, he was a Guest Editor for a special issue on therapeutic ultrasound of the IEEE Transactions on Ultrasonics, Ferroelectrics, and Frequency Control. From 1997 to 2002, he was an Associate Editor of the IEEE Transactions on Ultrasonics, Ferroelectrics, and Frequency Control. He is currently an Associate Editor of the IEEE Transactions on Biomedical Engineering. He is a member of the Standing Technical Program Committee for the IEEE Ultrasonics Symposium and a member of the Board of the International Society for Therapeutic Ultrasound.

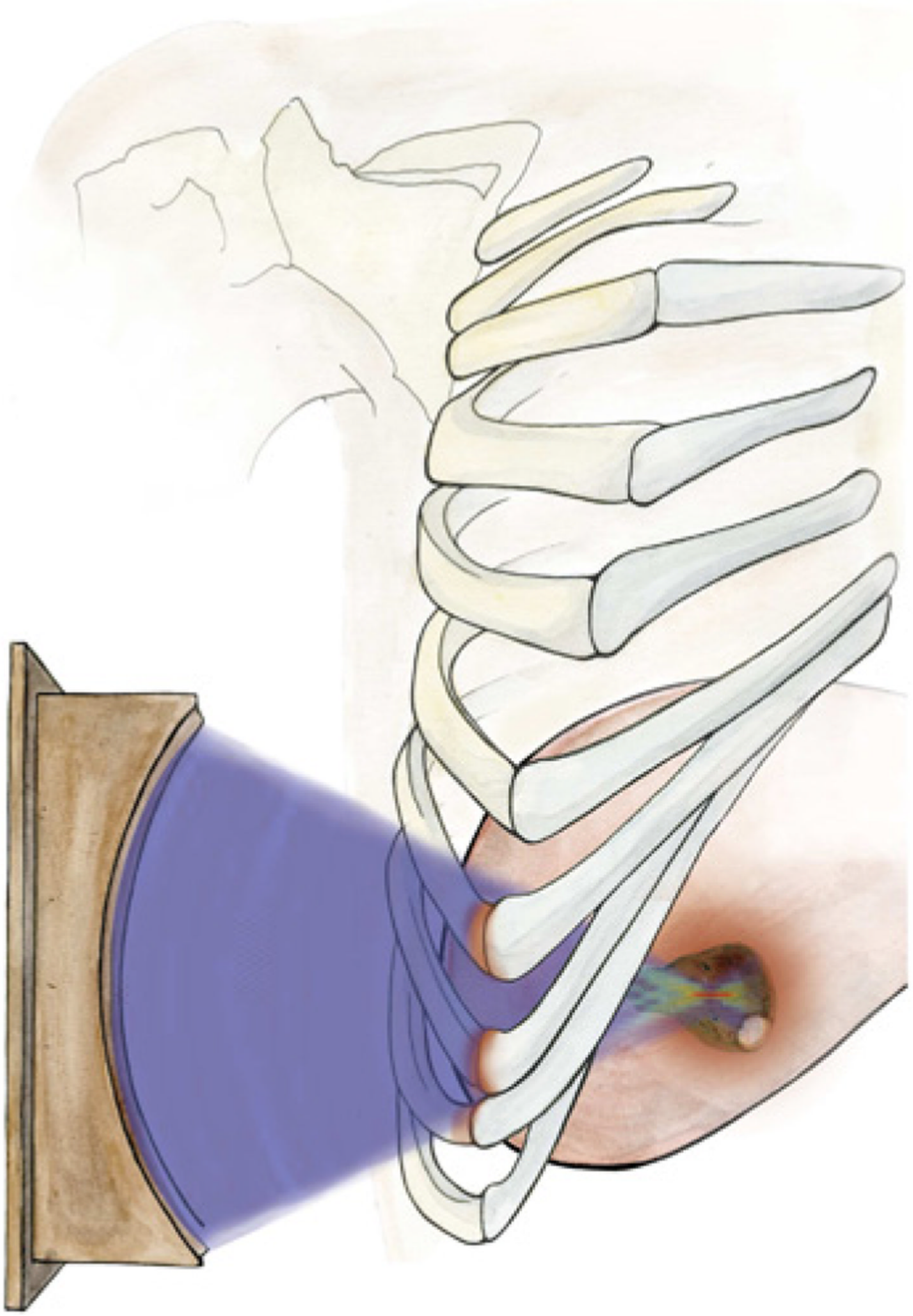

Fig. 1.

Medical illustration showing a geometric focused beam profile targeting a tumor in the liver. The beam is distorted due to the heterogenities of the rib cage, and thus causes undesirable heating across the ribs.

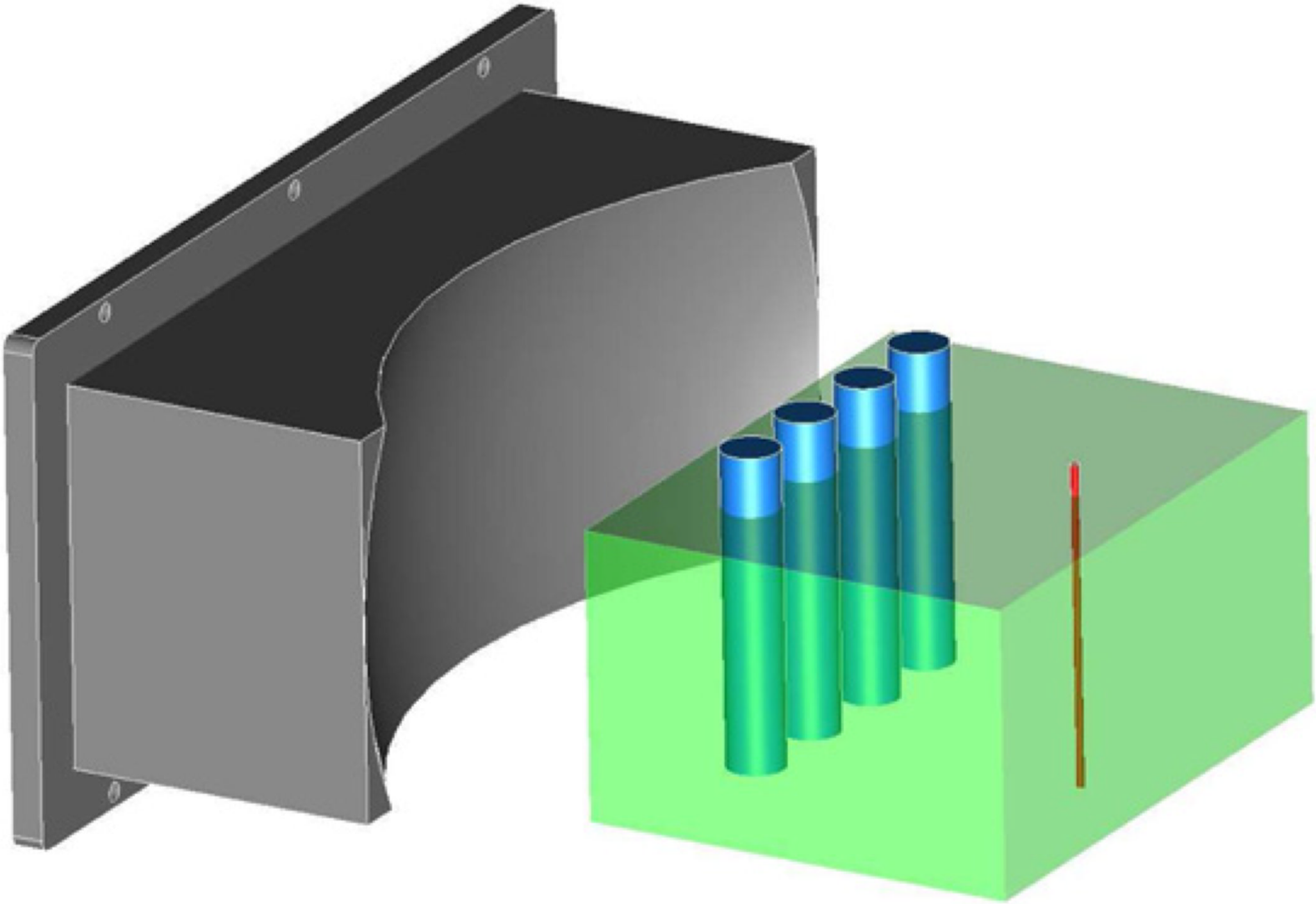

Fig. 2.

Experimental setup showing the position of the Plexiglas ribs within the tissue-mimicking phantom and a thermocouple placed at the target location.

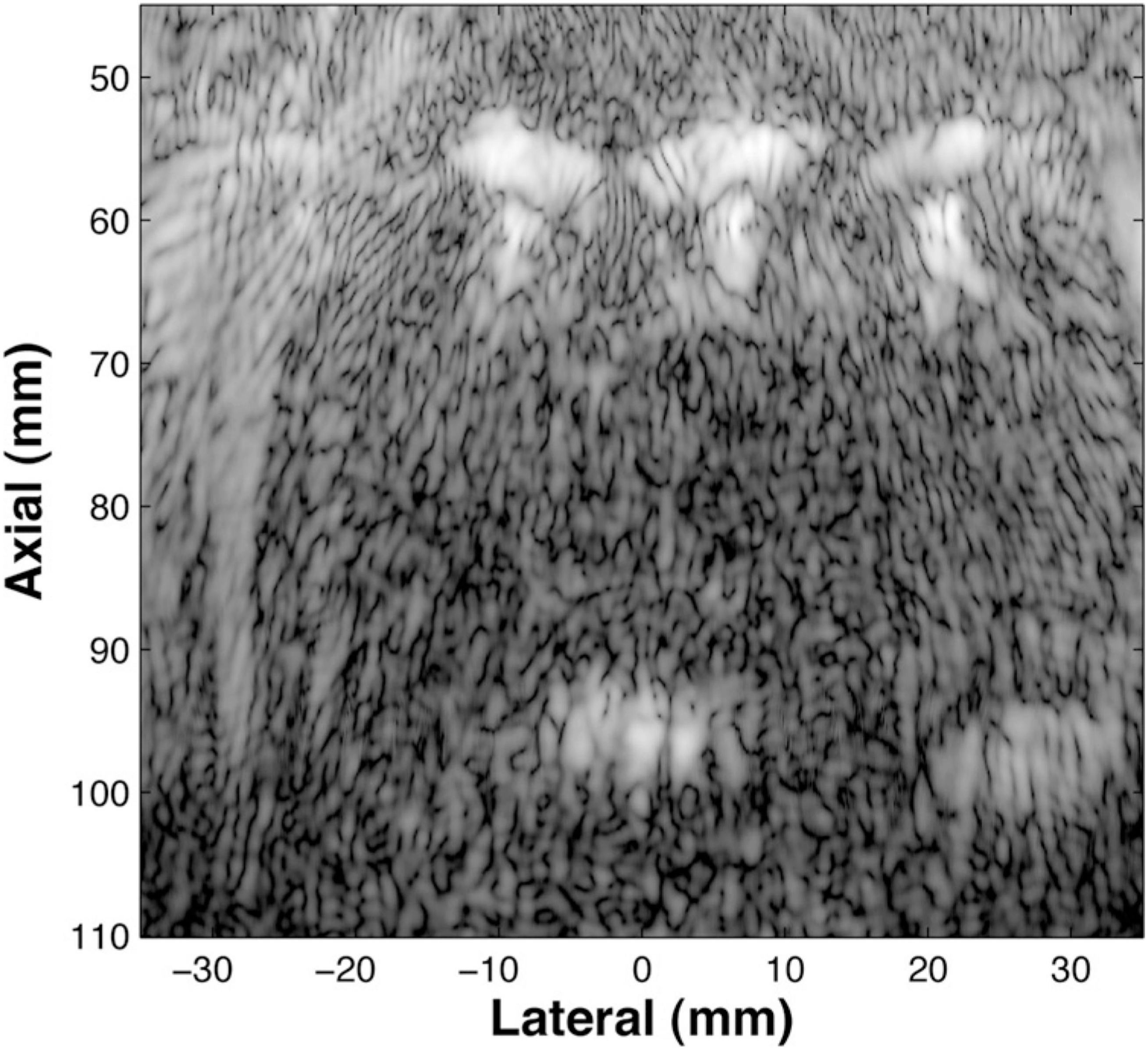

Fig. 3.
SA image (50 dB) of the tissue-mimicking phantom with embedded Plexiglas ribs and the target placed at (0, 100).

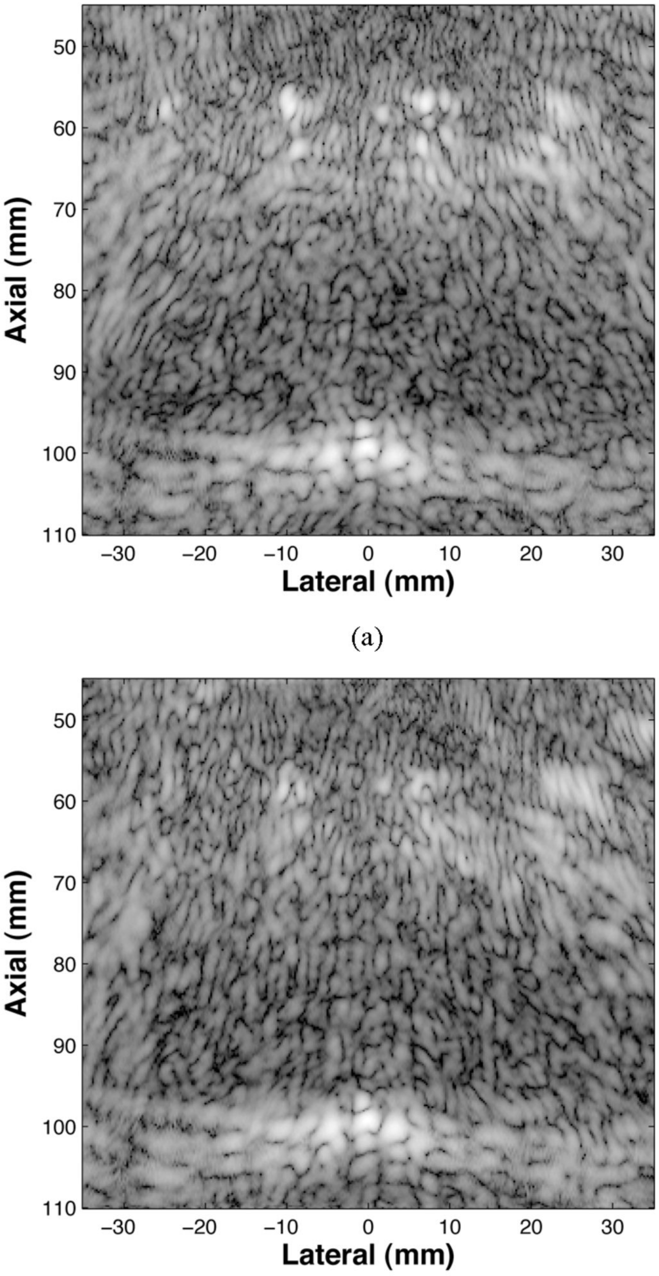

(a)

(b)

Fig. 4.

Normalized STF images (50 dB) of the target region utilizing (a) the geometrically focused HIFU beam and (b) the refocused HIFU beam obtained with the adaptive refocusing algorithm with the target placed at the geometric focus (0, 100) mm. (a) Geometrically focused. (b) Adaptively refocused.

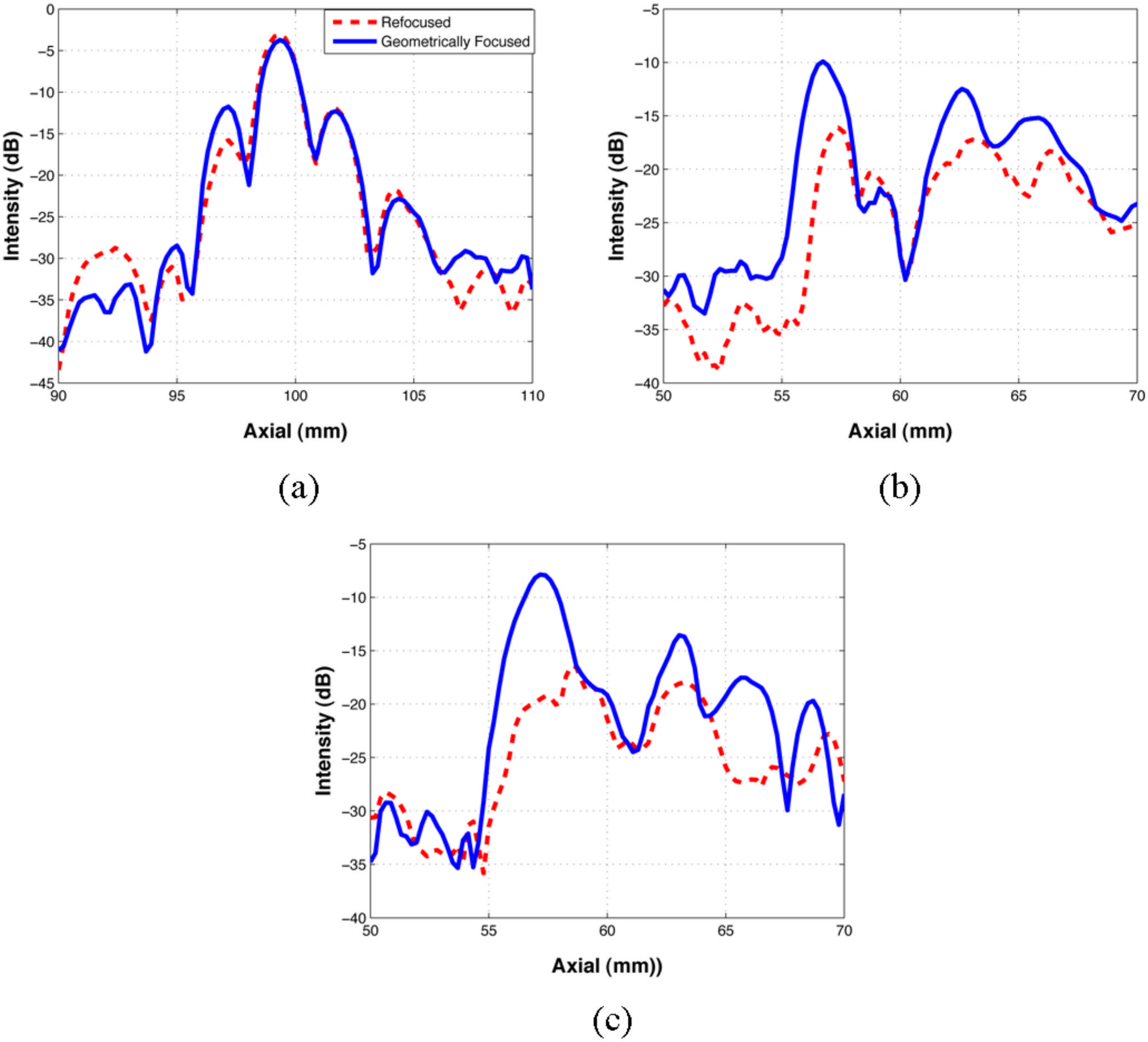

Fig. 5.

Echogenicity profiles along an axial line through (a) the target, (b) the middle right rib, and (c) the middle left rib are shown. The solid line and dashed lines are obtained from the geometrically focused and refocused images, respectively, when the target is placed at the geometric focus (0, 100) mm. (a) Target echogenicity. (b) Right rib echogenicity. (c) Left rib echogenicity.

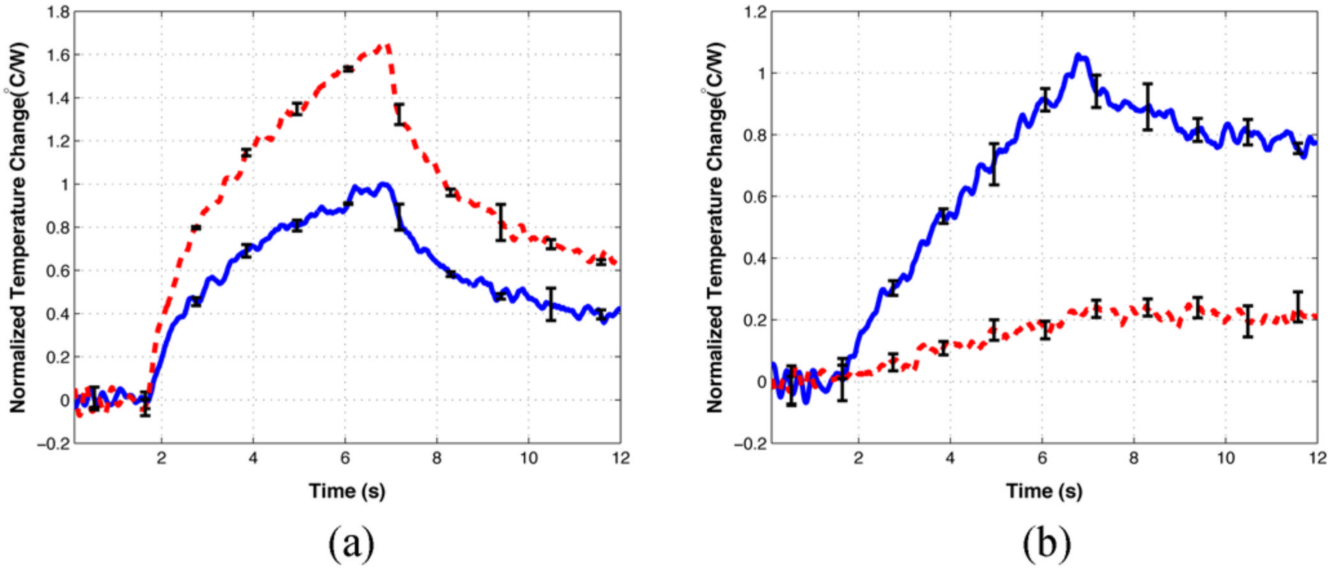

Fig. 6.

Normalized measured temperature change (bars indicate variance) at (a) the target location and (b) rib location for a 4-s HIFU exposure when the target was placed at the geometric focus (0, 100) mm. Normalization taken with respect to the maximum temperature at the target in response to the geometrically focused HIFU beam.

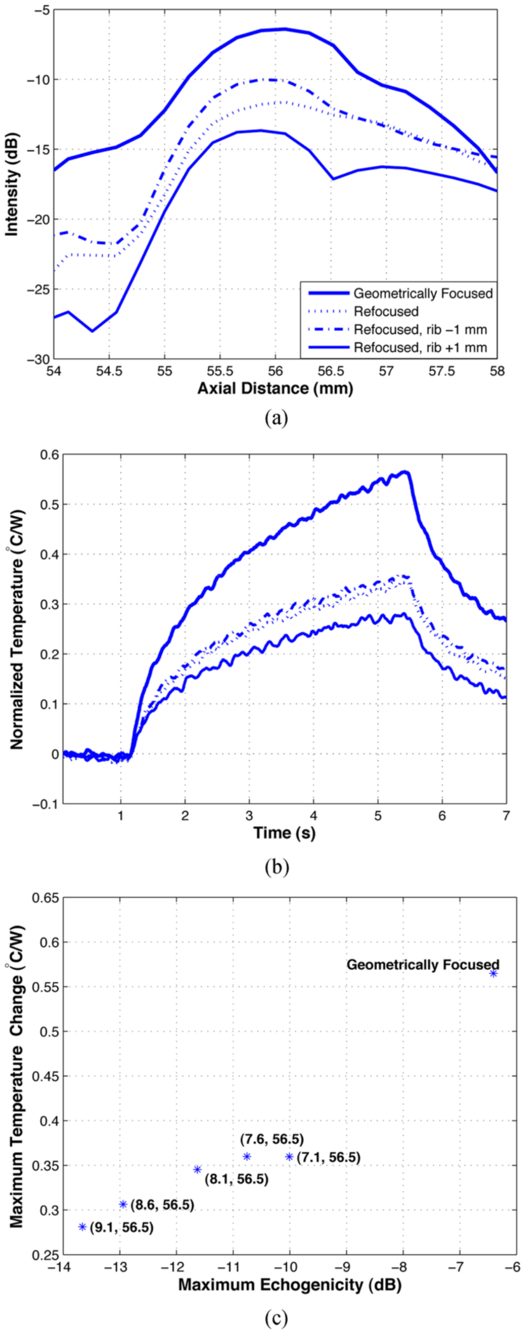

Fig. 7.

Effect of uncertainty of critical point selection for a target at (5, 100) mm. (a) and (b) Echogenicity and corresponding temperature profiles for the geometrically focused (thick solid), adaptively refocused (dotted), adaptively refocused with the critical point shifted by −1 mm (dashed-dotted) and by +1 mm (thin solid). (c) Maximum temperature plotted against the maximum echogenicity for the geometrically focused beam and five different critical point selections.

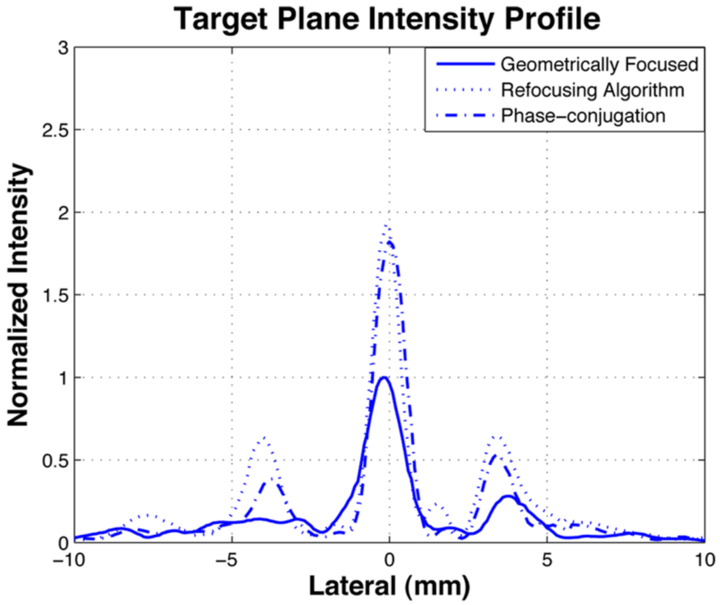

(a)

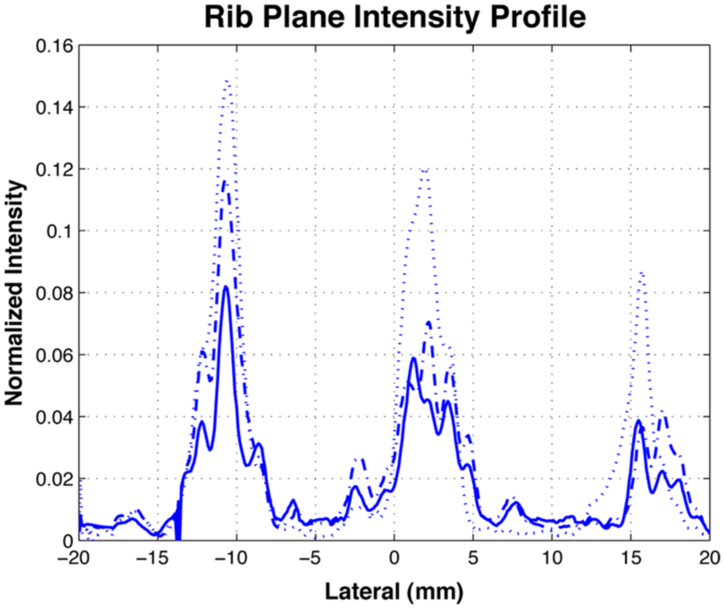

(b)

Fig. 8.

Field intensity profiles are plotted at (a) the target plane and (b) rib plane for the geometrically focused (solid line), refocused (dotted line), and the phase-conjugation (dashed-dotted line) HIFU beams.

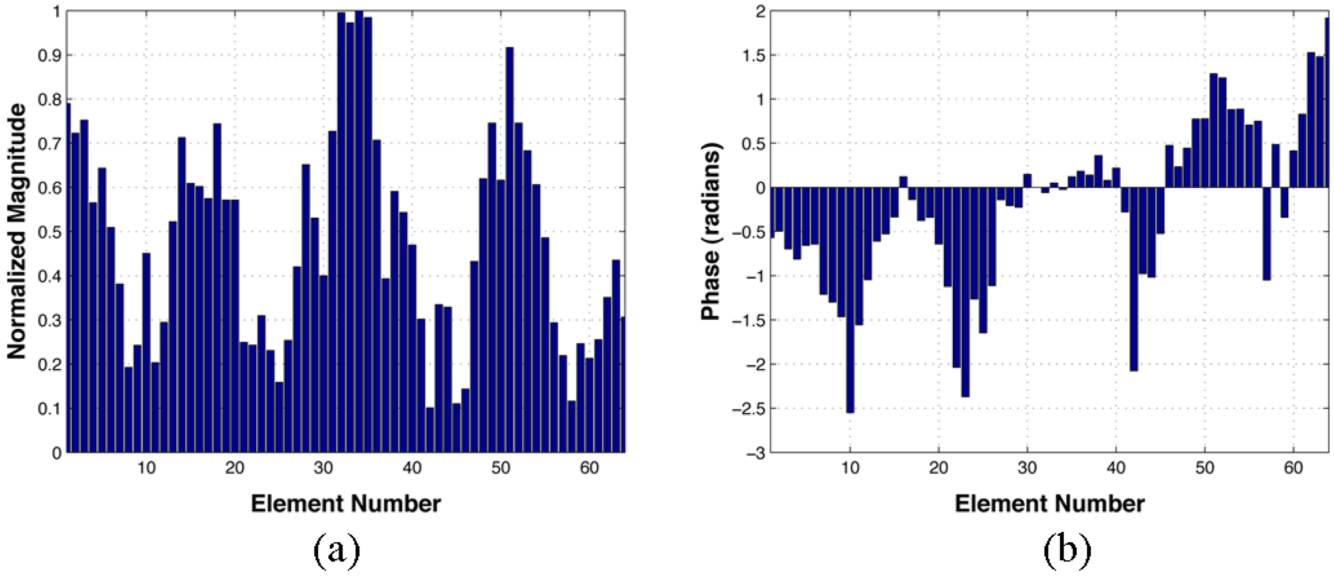

Fig. 9.

Magnitude and phase of the array excitation vector obtained from the adaptive refocusing algorithm.

TABLE I

Target to Rib Temperature and Echogenicity Ratios for the Six HIFU Beams Described in Section III-A1

Case (x_T,z_T)	**T_T/T_{Rib}**	**E_T/E_{rib} (dB)**	**ΔE (dB)**
Geometric Focusing (0,100)	0.94	4.1, 6.2	
Adaptive Refocusing (0,100)	6.7	14.3, 13.1	10.2, 6.9
Geometric Focusing (5,100)	1.8, 1.0	−14.8, −7.6	
Adaptive Refocusing (5,100)	3.8, 2.7	0.2, 12.1	15.0, 19.7
Geometric Focusing (10,100)	0.4, 0.6	−9.0, −10.9	
Adaptive Refocusing (10,100)	1.7, 2.9	1.6, −2.4	10.6, 8.5

Double entries are for right and left ribs, respectively.